

1 **Diagnosing Ozone-NO_x-VOCs-Aerosols Sensitivity and**
2 **Uncovering Causes of Urban-Nonurban Discrepancies in**
3 **Shandong, China using Transformer-Based Estimations**

4
5
6 *Chenliang Tao¹, Yanbo Peng^{1,2,*}, Qingzhu Zhang^{1,*}, Yuqiang Zhang¹, Bing*
7 *Gong³, Qiao Wang¹, Wenxing Wang¹*

8
9
10
11 ¹Big Data Research Center for Ecology and Environment, Environmental Research
12 Institute, Shandong University, Qingdao 266237, P.R. China

13 ²Shandong Academy for Environmental Planning, Jinan 250101, P.R. China

14 ³Jülich Supercomputing Centre, Forschungszentrum Jülich, 52425 Jülich, Germany

15
16
17 **Keywords:**

18 Air pollution, Deep learning, Transformer, Satellite, Urban-rural difference, Ozone Regime

19 _____
20 *Corresponding authors. E-mail: zqz@sdu.edu.cn, pengyanbo@mail.sdu.edu.cn

21 **Abstract**

22 Narrowing surface ozone disparities between urban and nonurban areas escalate health
23 risks in densely populated urban zones. A comprehensive understanding of the impact
24 of ozone photochemistry on this transition remains constrained by current knowledge
25 of aerosol effects and the availability of surface monitoring. Here we reconstructed
26 spatiotemporal gapless air quality concentrations using a novel Transformer deep
27 learning (DL) framework capable of perceiving spatiotemporal dynamics to analyze
28 ozone urban-nonurban differences. Subsequently, the photochemical effect on these
29 discrepancies was analyzed by elucidating shifts in ozone regimes inferred from an
30 interpretable machine learning method. The evaluations of model exhibited an average
31 out-of-sample cross-validation coefficient of determination of 0.96, 0.92, and 0.95 for
32 ozone, nitrogen dioxide, and fine particulate matter (PM_{2.5}), respectively. The ozone
33 sensitivity in nonurban areas, dominated by nitrogen oxide (NO_x)-limited regime, was
34 observed to shift towards increased sensitivity to volatile organic compounds (VOCs)
35 when extended to urban areas. A third ‘aerosol-inhibited’ regime was identified in the
36 Jiaodong Peninsula, where the uptake of hydroperoxyl radicals onto aerosols
37 suppressed ozone production under low NO_x levels during summertime. The reduction
38 of PM_{2.5} would increase the sensitivity of ozone to VOCs, necessitating more stringent
39 VOC emissions abatement for urban ozone mitigation. In 2020, urban ozone levels in
40 Shandong surpassed those in nonurban areas, primarily due to a more pronounced
41 decrease in the latter resulting from stronger aerosol suppression effects and lesser
42 PM_{2.5} reductions. This case study demonstrates the critical need for advanced spatially
43 resolved models and interpretable analysis in tackling ozone pollution challenges.

44

1. INTRODUCTION

Surface ozone (O_3), fine particulate matter ($PM_{2.5}$), and nitrogen dioxide (NO_2) are among the most important trace gases in the atmosphere that significantly impact the ecological environment and public health (Han and Naeher, 2006; Yue et al., 2017). During the Action Plan on the Prevention and Control of Air Pollution (denoted as the Clean Air Action, 2013-2017) (Action Plan on Air Pollution Prevention and Control (in Chinese), 2023), $PM_{2.5}$ and nitrogen oxide (NO_x = nitric oxide (NO) + NO_2) emissions across China decreased by 33% and 21%, respectively (Zheng et al., 2018), while surface O_3 exhibited an increasing trend (Lu et al., 2018). The increase in O_3 could be partially attributed to the “aerosol-inhibited” effect, where the reduction in $PM_{2.5}$ results in a diminished reactive uptake of hydroperoxyl radicals (HO_2) onto aerosols (Ivatt et al., 2022; Li et al., 2019). The societal benefits of reducing premature deaths and economic losses from $PM_{2.5}$ reductions have been diminished by the rising O_3 (Liu et al., 2022). Thus, achieving the joint attainment objectives for $PM_{2.5}$ and O_3 has been put on the top priority of China’s long-term air pollution control policies.

The complexity of the O_3 formation is partly reflected by the nonlinear response to changes in precursors (i.e. volatile organic compounds (VOCs) and NO_x), as well as the presence of heterogeneous reactions in aerosols. Understanding these dynamics is crucial to investigate current narrowing differences in O_3 concentrations between urban and nonurban areas, which have traditionally shown higher levels in rural (Han et al., 2023). The formaldehyde-to- NO_2 ratio ($HCHO/NO_2$ or FNR) serves as a theoretical

66 gauge of the relative abundance of total organic reactivity to hydroxyl radicals (OH)
67 and NO_x (Wei et al., 2022c; Sillman, 1995), and as such, it can function as a useful
68 indicator of O₃ sensitivity. Previous studies have utilized the HCHO/NO₂ from satellite
69 remote sensing to infer O₃ production regimes for guiding O₃ control policies (Jin et al.,
70 2023; Li et al., 2021a; Jin et al., 2020). However, the changes of HCHO/NO₂ threshold
71 in O₃ regimes classification modulated by meteorology and localized atmospheric
72 chemistry in space and time, and uncertainties relating column to surface, precluding
73 robust applications over larger spatial scales (Lee et al., 2023; Jin et al., 2017; Sourì et
74 al., 2023). While the observation-based model method alleviates some of these
75 limitations, constraints remain including computational demands and priori chemical
76 mechanisms (Song et al., 2022b; Chu et al., 2023). The advent of interpretable machine
77 learning models affords new opportunities to unravel intricate dependencies governing
78 O₃ formation purely from actual observational data. However, sparse ground-based
79 monitoring stations, especially in rural areas, pose great challenges to the spatially full
80 coverage of studies. Thus, the high-spatiotemporal-resolutions estimations of surface
81 air pollutants are urgently needed to improve our understanding of how these pollutants
82 are changing and interacting.

83 Recent studies have utilized spatially resolved remote sensing data to estimate the
84 continuous distribution of air pollutants in space by diverse machine learning (ML)
85 models (Lyapustin and Wang, 2022; Lamsal et al., 2022; Huang et al., 2021; Li and
86 Wu, 2021; Ren et al., 2022b), such as random forest (RF), full residual deep learning,

87 and Bayesian ensemble model. These attempts have demonstrated the tremendous
88 potential of machine learning as an alternative to atmospheric chemical models (Jung
89 et al., 2022). Nevertheless, there are still several aspects that have not been fully
90 considered. For instance, coarse-resolution maps limit the ability to characterize the
91 fine-scale variation of air pollution within urban areas, which has significant
92 implications for environmental justice disparities of disadvantaged communities
93 (Jerrett et al., 2005; Ren et al., 2022b; Dias and Tchepel, 2018). Additionally, existing
94 ML models may not fully account for the complex atmospheric chemistry and physics
95 processes that influence pollutant concentrations due to the single-pixel-based
96 processing mode (Huang et al., 2021; Requia et al., 2020; Thongthammachart et al.,
97 2022; Li et al., 2022b; Geng et al., 2021). Although several efforts have been made by
98 using the neural network with convolutional layers (Di et al., 2016), and explicitly
99 incorporating spatiotemporally weighted information to machine learning models (Wei
100 et al., 2022b), the global spatiotemporal self-correlation of multi-dimensional features
101 in the input array remained unaddressed. Meanwhile, the convolutional operations
102 extract features from all neighboring grids of the target, ignoring the fact that the
103 environmental knowledge of the target grid itself is the most significant, with the
104 adjacent features being secondary.

105 In this study, we aim to analyze the evolving dynamics of urban-nonurban O₃
106 differences between 2019 and 2020. The roles of emission discrepancies and
107 nonlinearity of O₃-NO_x-VOCs-aerosols photochemical processes in shaping these O₃

108 variations were deeply dissected. To achieve a comprehensive analysis, we employed a
109 new spatiotemporal Transformer framework that paid special attention to air mass
110 transport and dispersion affected by the spatial-temporal correlations, to reconstruct the
111 spatially gapless air quality datasets based on satellite data, ground-level observations,
112 and meteorological reanalysis. The estimations are particularly vital for regions lacking
113 dense ground-based monitors, ensuring that our understanding of O₃ dynamics in urban-
114 nonurban areas and formation regimes is not limited by geographical constraints in data
115 availability. Surface O₃ formation regimes in Shandong province were inferred by the
116 classic XGBoost model (Chen and Guestrin, 2016) coupled with Shapley Additive
117 exPlanations (SHAP) (Lundberg and Lee, 2017), which identifies the impact of
118 meteorological conditions and photochemical indicators (i.e. PM_{2.5} as a proxy for
119 aerosols, NO₂ as a proxy for NO_x, and HCHO as a proxy for VOCs) on O₃. The
120 innovative Transformer-based modeling and interpretable machine learning analysis
121 approaches are expected to enable new applications such as those of air quality
122 simulation and O₃ formation regimes studies.

123 **2. MATERIALS AND METHODS**

124 **2.1 Predictor Variables**

125 The study domain covered the Shandong province of China, which has a high
126 mortality burden of air pollution (Liu et al., 2017). The surface PM_{2.5}, O₃, and NO₂
127 concentration measurements were collected from the regulatory air quality stations of
128 the China National Environmental Monitoring Center (CNEMC, with a total of 179

129 locations) and the Shandong Provincial Eco-environmental Monitoring Center (SDEM,
130 with a total of 166 locations) (Figure S1). The SDEM stations were included to fill the
131 spatial gaps in the county and rural areas where CNEMC stations were lacking. The
132 study area was divided into 1.22 million grid cells with a spatial resolution of 500
133 meters. We utilized a range of predictor data, including tropospheric NO₂ vertical
134 column densities (VCDs) and O₃ total VCDs measured by TROPospheric Monitoring
135 Instrument (TROPOMI) (Lamsal et al., 2022; Copernicus Sentinel-5P (processed by
136 ESA), 2020), aerosol optical depth (AOD) data and atmospheric properties obtained
137 from Moderate Resolution Imaging Spectroradiometer (MODIS) Multi-Angle
138 Implementation of Atmospheric Correction products (Lyapustin and Wang, 2022),
139 AOD estimates from Modern-Era Retrospective Analysis for Research and
140 Applications as the supplement to MODIS (2015), meteorological reanalysis obtained
141 from the fifth generation atmospheric reanalysis dataset of European Centre for
142 Medium-Range Weather Forecasts (ECMWF) (ERA5) (Hersbach et al., 2023, p.5),
143 daily dynamic industrial emissions, moonlight-adjusted nighttime lights product
144 (Román et al., 2018), vegetation index (Didan, 2021), population density (WorldPop,
145 2018), road density, land use data (Jun et al., 2014), and the shuttle radar topography
146 mission digital elevation model. The detailed information for all predictive variables
147 is listed in Table S1 and discussed in Text S1-2. Taking space-variant and seasonal
148 patterns into consideration, several spatiotemporal indicators such as geographical
149 coordinates, Euclidean spherical coordinates, year, Julian date, and helix-shaped

150 trigonometric sequences₂ were also included as predictor variables (Text S3) (Sun et al.,
151 2022). Geographic Information Systems techniques₂ including reprojection and
152 resampling₂ were used to consolidate all the data obtained for consistent projection and
153 spatial scale. Finally, the Light Gradient Boosting Machine was used to fill satellite data
154 gaps (Text S4) (Ke et al., 2017).

155 2.2 Air Transformer

156 AiT is an individual Transformer model that adopts an encoder-decoder
157 architecture with multidimensional self-attention computation to dynamically capture
158 the spatiotemporal autocorrelation of atmospheric pollution changes from the
159 sequences of pixels and variables for more reliable spatial maps of estimation.
160 Compared with existing image and video recognition Transformers, such as ViT
161 (Dosovitskiy et al., 2021), Timesformer (Bertasius et al., 2021)₂ and Uniformer (Li et
162 al., 2021b), AiT is innovative in incorporating self-attention across channels after the
163 pixels-based self-attention and taking advantage of the decoder. The former can capture
164 the correlations between predictor variables. The decoder was employed to enable
165 interaction between the primary target grid and neighboring grids. Predictor variables
166 with 8 timesteps within 1000 meters of the target grid cell were fed into the model to
167 learn spatiotemporally disparities among atmospheric pollutants for predicting O₃, NO₂
168 and PM_{2.5} within the target grid point.

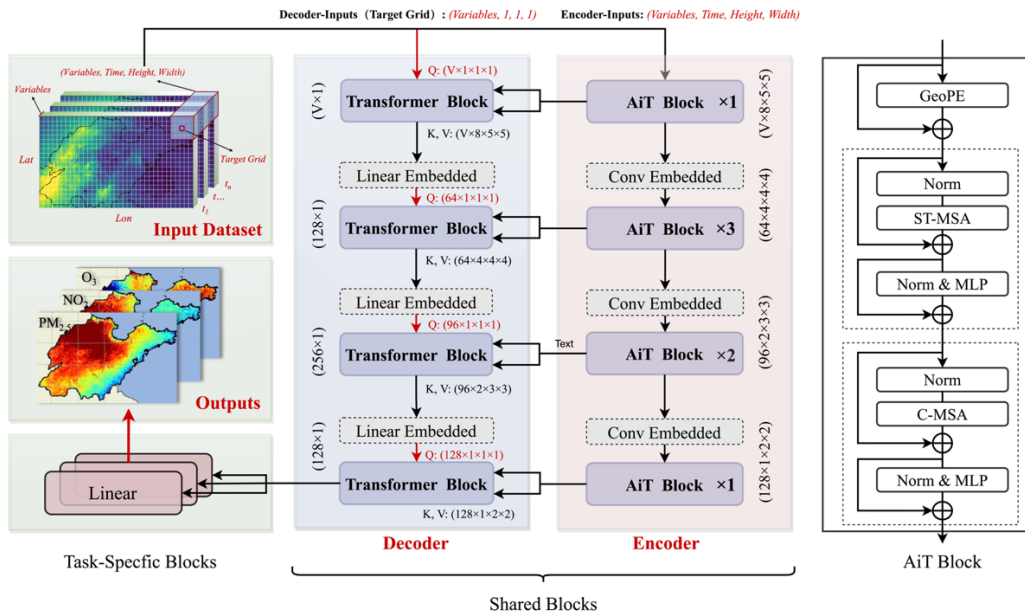
169 The overall architecture of the proposed AiT model and the dimensions of input
170 data are illustrated in **Figure 1**. The encoder maps an input sequence with neighborhood

171 spatiotemporal data to a sequence with high-dimensional spatiotemporal characteristics,
 172 and the decoder generates an estimation by computing self-attention representations
 173 between the target grid and outputs of the encoder. The encoder of AiT takes as input a
 174 clip $X \in R^{V \times T \times H \times W}$ consisting of T multi-variable frames of size $H \times W$ sampled
 175 from the original dataset, where V is the number of variables and the target grid cell is
 176 located at $(\lfloor \frac{H}{2} \rfloor, \lfloor \frac{W}{2} \rfloor)$. The decoder takes as input a clip $X \in R^{V \times 1 \times 1 \times 1}$ consisting of V
 177 variables from the target grid. Several Transformer blocks with modified self-attention
 178 computation (AiT blocks) are applied to the encoder. The AiT encoder block is similar
 179 to the standard vision transformer block but specifically designed for atmospheric
 180 estimation (Dosovitskiy et al., 2021). It is a stack of two self-attention schemes,
 181 including global spatiotemporal self-attention on the pixels and channel self-attention
 182 on variable predictors. The former contains $N = HW$ effective input sequence length
 183 for the self-attention to extract spatiotemporal information. The latter computes self-
 184 attention based on V effective input sequence length to capture hidden information on
 185 variables. The decoder part is symmetric to the encoder part, but it only has a block
 186 with the spatiotemporal self-attention mechanism. We compute the matrix of self-
 187 attention outputs as:

$$188 \quad \text{Attention}(Q, K, V) = \text{softmax}\left(\frac{QK^T}{\sqrt{d_k}} + B\right)V \quad (1)$$

189 where Q , K , and V are the queries, keys, and values in the inputs of the particular
 190 attention, respectively. d_k is the feature dimensionality of K , and B is the geographic
 191 positional bias term. Another difference is that the attention function of the decoder is

192 computed on Q from the estimated grid data, and (K, V) from the outputs of encoder
 193 blocks under the same stage, resulting in the outputs of the last decoder block being
 194 sized 1×128 . The description of the data transformation and design details in the
 195 process of training can be found in Text S5. The multi-task learning strategy was also
 196 applied for learning representation across multiple pollutant estimation tasks (Text S6).
 197 The aggregated feature data from June 2019 to June 2021 were utilized to train and
 198 validate the model through cross-validation (CV), where the optimal model, trained
 199 based on out-of-sample CV, was used to estimate multiple pollutant concentrations
 200 during the study period, which was then employed for subsequent analysis.



201
 202 **Figure 1.** Schematic diagram of the AiT model. The white box of multi-dimension
 203 inputs presents each pixel of raster data. The AiT Block is a Transformer block based
 204 on self-attention across space, time, and variables. The GeoPE, Norm, MLP, ST-MSA
 205 and C-MSA indicate respectively positional embedding, layer normalization, multi-
 206 layer perceptron, spatial-temporal multi-head self-attention and multi-channels (multi-
 207 variables) multi-head self-attention.

208 2.3 Diagnosing O₃ Formation Sensitivity

209 Interpretability can provide insight into how a model may be improved, bolster the
210 understanding of the process being modeled, and engender appropriate confidence
211 among researchers. SHAP is a coalitional game-theoretic approach based on Shapley
212 values (Shapley, 1988) and then assigns each variable an importance value for a
213 particular estimation. Deep SHAP, a high-speed approximation algorithm that builds on
214 the connection between Shapely values and DeepLIFT (Shrikumar et al., 2019), is
215 employed to compute the feature importance of AiT from all data with monitoring
216 labels for interpreting the prediction. The sensitivity of the O₃ formation regime was
217 deduced using a combination of the XGBoost model and SHAP interpretability method,
218 employing the GPUPtreeShap algorithm (Mitchell et al., 2020), which simulated the
219 response of surface O₃ to meteorological conditions, HCHO, NO₂ and PM_{2.5}, by
220 utilizing the continuous estimations from ERA5, AiT and TROPOMI between 2019 and
221 2020. The incorporation of meteorology in the model ameliorated the inadequacies in
222 the conventional method (HCHO-NO₂ ratio), where its thresholds for identifying O₃
223 regimes vary temporally and spatially. The positive or negative contributions of three
224 atmospheric pollutants were used to identify their promoting or inhibitory effects on O₃
225 variability. Given the unbiased property of SHAP values regarding directionality, the
226 normalized relative magnitudes of SHAP values were calculated for HCHO, NO₂ and
227 PM_{2.5}. This allowed the differentiation of the O₃ formation regimes based on the locally
228 maximal proportions of the SHAP values for each species. The ground-level monthly

229 HCHO concentrations were derived using a combination of column-to-surface
230 conversion factor (CF) simulated from the ECMWF Atmospheric Composition
231 Reanalysis 4 and the tropospheric HCHO VCDs obtained from TROPOMI (Cooper et
232 al., 2022; Su et al., 2022; Inness et al., 2019). A detailed description of the CF method
233 as used here is discussed in Text S7. To ensure consistency in resolution between
234 TROPOMI and AiT, we employed the oversampling method to downscale the
235 TROPOMI VCDs to the resolution of AiT estimation, which has been proven effective
236 in achieving finer resolution (Su et al., 2022; Cooper et al., 2022; van Donkelaar et al.,
237 2015).

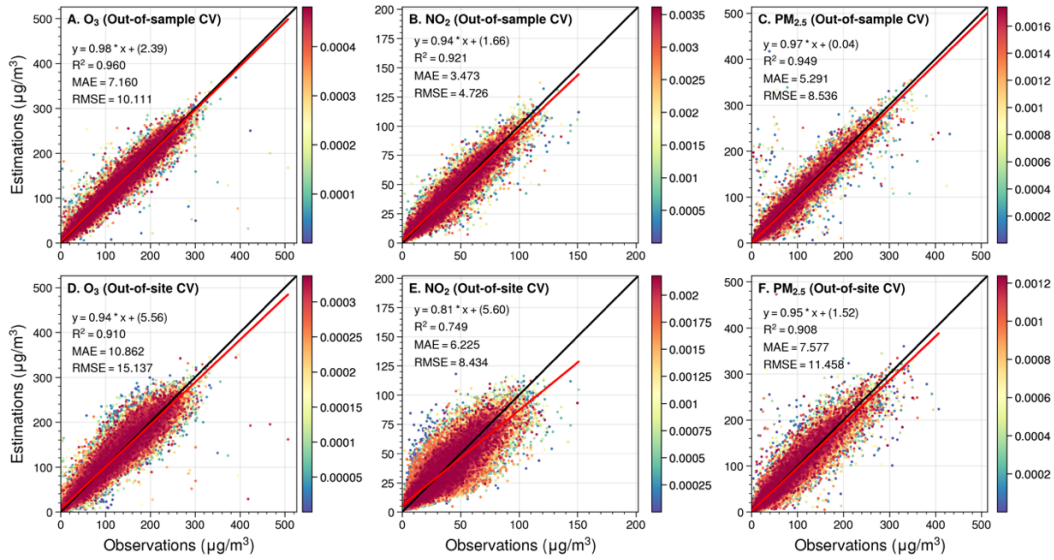
238 **3. RESULTS AND DISCUSSION**

239 **3.1 Performance Evaluation for the AiT**

240 **3.1.1 Cross-validation Metrics**

241 We evaluated the AiT performance using the 10-fold CV approach (Text S8), with
242 correlation coefficient (R^2) measuring the extent to which model simulations explain
243 variability in atmospheric pollutants, and root mean square errors (RMSE) and mean
244 absolute errors (MAE) evaluating the bias/error of the estimates. As shown in **Figure**
245 **2**, out-of-sample CV daily ground-level O_3 , $NO_{2,x}$ and $PM_{2.5}$ estimations are highly
246 consistent with ground observations ($R^2 = 0.96, 0.92, 0.95$), indicating low uncertainties,
247 with RMSE of 10.1, 4.7, and 8.5 $\mu\text{g}/\text{m}^3$ and MAE of 7.2, 3.5, and 5.3 $\mu\text{g}/\text{m}^3$ for the
248 2018-2021 period. The linear regression comparing the O_3 predictions versus
249 observations yields a slope of 0.98 and an intercept of 2.39, which demonstrates that

250 there is no systematic bias in the estimations. Meanwhile, as shown in Figure S3, our
251 AiT model performs well at the individual-site scale with high CV-RMSE for O₃, NO₂,
252 and PM_{2.5} (10.5 ± 8.6 , 4.7 ± 1.1 , and 8.3 ± 2.8 $\mu\text{g}/\text{m}^3$). In general, the AiT model is
253 robust for multi-pollutant simultaneous estimations.



254
255 **Figure 2.** Out-of-sample cross-validation (A-C) and out-of-site cross-validation (D-F)
256 of daily ground-level O₃, NO₂ and PM_{2.5} concentration in the validation set.

257 The spatial generalization ability of the AiT is then examined by the out-of-site CV
258 evaluation method (**Figure 2**). The daily spatial variations of O₃, NO₂, and PM_{2.5} at
259 locations without ground measurements can be well estimated by our model (i.e., CV-
260 $R^2 = 0.91, 0.75, 0.91$), representing a core contribution of such studies. We also probe
261 the model performance for each site separately based on spatial CV estimations (Figure
262 S4). This general model yields an RMSE of 15.2 ± 8.8 , 8.1 ± 2.7 , and 11.1 ± 2.8 $\mu\text{g}/\text{m}^3$,
263 respectively. Furthermore, we trained the AiT model using data exclusively from
264 CNEMC and assessed its generalizability by validating it with data from SDEM. The

265 model demonstrates strong performance with high our-of-sample CV R^2 values in the
266 validation dataset of CNEMC (Figure S5), and when evaluated with SDEM data, it
267 exhibits only an acceptable degradation in predictive accuracy (Figure S6, R^2 for O₃,
268 NO₂, and PM_{2.5}: 0.90, 0.73, 0.79). Meanwhile, our framework utilizes multi-task
269 learning to enhance computational efficiency through a single iteration and leverages
270 the interactions among multiple pollutants to optimize the performance at individual
271 pollutant levels (Table S2). In summary, AiT provides relatively stable estimations in
272 areas without available ground-level monitoring and reliably extends ground
273 monitoring from the site scale to the full-coverage spatial scale with high spatial
274 resolution.

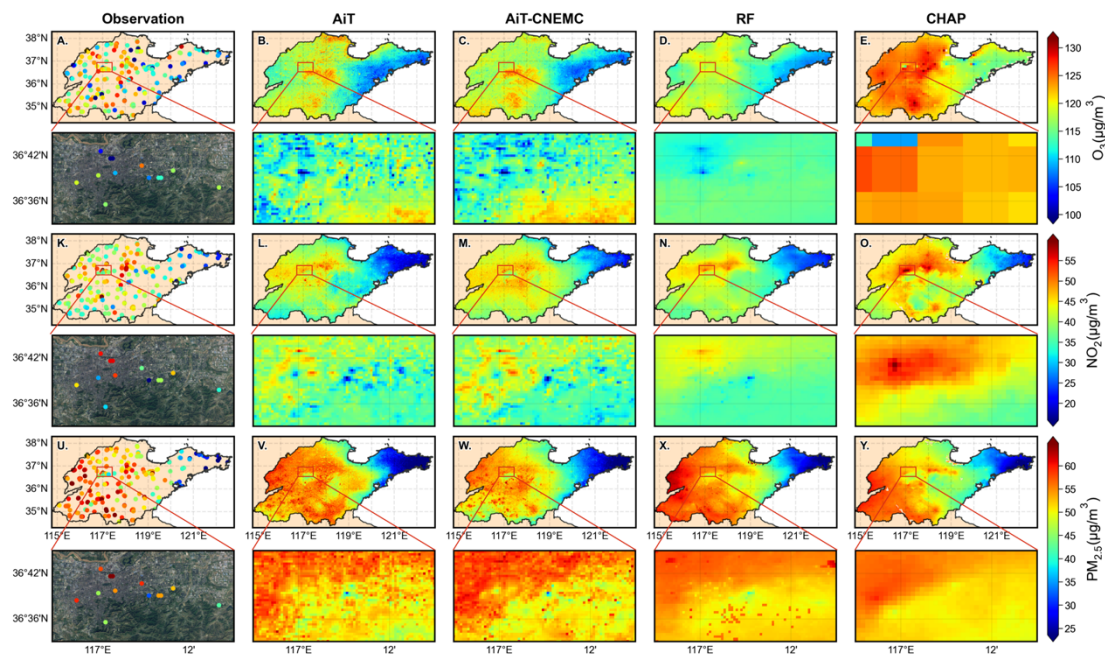
275 **3.1.2 Compared with Other ML Models**

276 Since ground-level air quality measurements across the target regions are
277 extremely limited at a 500 m spatial resolution, representing only roughly two-
278 thousandths of the total grid cells, we seek implicit approaches to validate our estimated
279 near surface pollutant concentrations. We compared the model performance with
280 previous studies that applied different ML methods to estimate these three air pollutants
281 individually and found out that our cross-validation results are comparable or even
282 better than those (Table S3). We also created a new dataset in our study by applying the
283 classic RF algorithm which is the most common ML model for estimating atmospheric
284 pollution in recent years (Wei et al., 2022a; Requia et al., 2020; Xiao et al., 2018; Geng
285 et al., 2021; Lu et al., 2021) with the same variables as AiT. The statistical comparisons

286 between AiT and RF are also shown in Table S3. We then compared the spatial
287 distribution of our results with estimations from CHAP, AiT-CNEMC, and RF.

288 **Figure 3** shows the spatial maps of near-surface air pollutants with partially
289 zoomed satellite images for monitoring sites, AiT, CNEMC-trained AiT, RF, and CHAP
290 in 2019 (see Figure S7 for 2020). We found that the estimated NO₂ and PM_{2.5} from the
291 AiT share a similar spatial distribution to those estimated by RF and CHAP. However,
292 enlarged city-level urban regions in **Figure 3** reveal that AiT estimates fine structures
293 and intra-urban disparities in near-surface multi-pollutant concentrations, which cannot
294 be captured by either RF or CHAP products. This spatial gradient is also captured by
295 AiT trained with CNEMC data, revealing the reliability of the deep learning model
296 structure. In general, while RF and CHAP can only identify the hotspots of air pollutants
297 at a regional scale, the spatial distribution of air pollutants estimated by AiT shows
298 much more detailed differences with high spatial and temporal variability across the
299 city scale. The differences of near-surface annual averaged pollutants between 2019 and
300 2020 for measured and multi-estimated data are presented in Figure S8. The reductions
301 or increases of O₃, NO₂, and PM_{2.5} in distinct locations can be simulated by our model,
302 which is relatively consistent with the changes of measurements. The zoomed maps in
303 Figure S7 show the differences in three pollutant concentrations at the city scale of the
304 capital of Shandong Province, Jinan. It can be found that the change in pollutant levels
305 in 2020 compared to 2019 exhibits substantial regional variations and intra-urban
306 heterogeneity, with some areas experiencing an increase while others a decrease.

307 Compared to the estimations of RF and CHAP, our results successfully capture the
 308 complex distribution of air pollution in reality and reveal that the decline in PM_{2.5} is
 309 primarily concentrated in suburban areas, while an increase is pronounced in some
 310 regions of urban during 2020. Notably, this spatial trend may be consistent with
 311 underlying emission patterns and meteorological conditions.



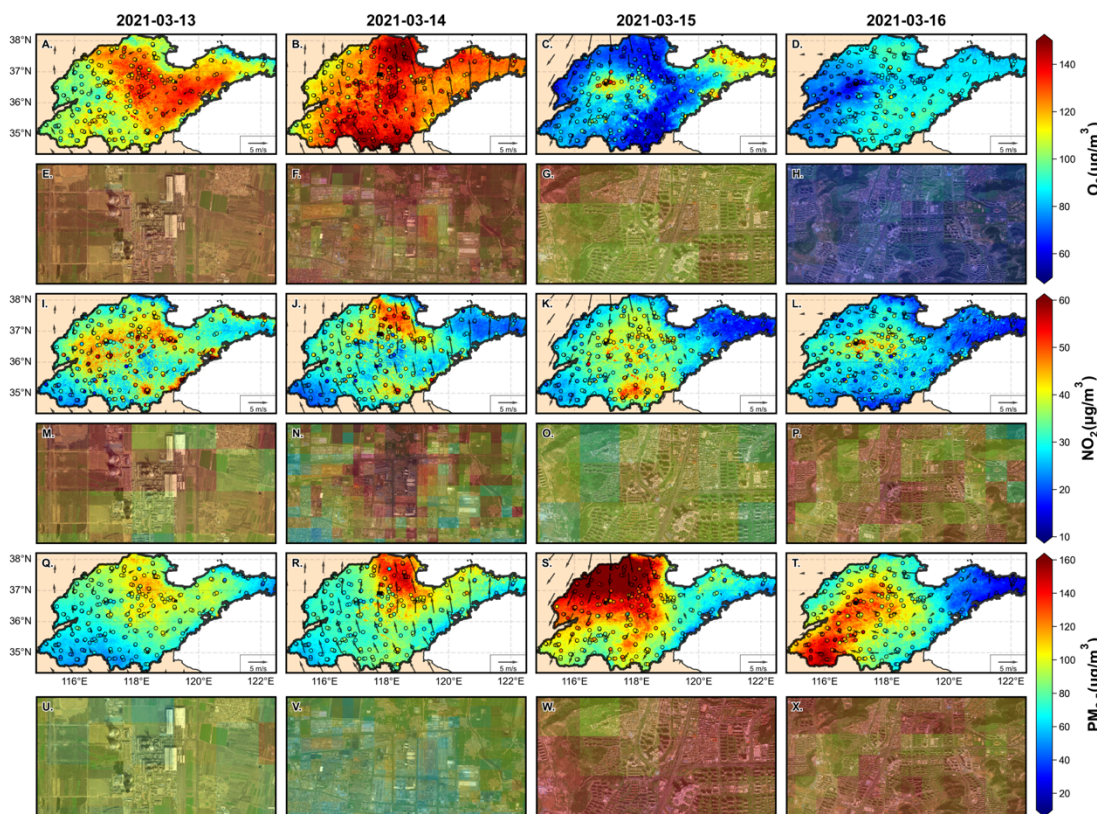
312 **Figure 3.** Spatial distribution of the annual mean (A-E) O₃, (K-O) NO₂ and (U-Y)
 313 PM_{2.5} concentrations from observations, Air Transformer (AiT), CNEMC-trained AiT,
 314 Random Forest (RF) and ChinaHighAirPollutants (CHAP), respectively, in 2019. The
 315 region enclosed by the red rectangular box corresponds to the zoomed-in maps of the
 316 satellite (© Tianditu: www.tianditu.gov.cn) and pollutant concentrations at a city scale
 317 for the capital city of Shandong Province, Jinan.

319 3.1.3 Typical Event Study

320 The typical example of the spatial distribution of multi-pollutant observations and
 321 estimations of AiT is compared for validating the predictive capability of the model at

322 a particular pollution episode, i.e., 13-16 March 2021. During this period, an early
323 season dust storm, which was called the largest and strongest such storm in a decade,
324 hits northern China (Myers, 2021). As shown in **Figure 4**, our model can capture the
325 spatial distribution of surface O₃, NO₂, and PM_{2.5} in the time of severe atmospheric
326 pollution. In addition, our estimations are in high concordance with measurements in
327 terms of magnitudes and spatial variability over the entire research region. The model
328 trained solely on CNEMC data is also capable of effectively capturing the drastic
329 changes in air quality during the pollution episode (Figure S9). Combining wind fields
330 to analyze PM_{2.5} distribution on the day of the dust storm, it can be found that surface
331 wind carries a massive amount of particulate matter from Beijing, which suffered a
332 severe dust storm, to northern Shandong. The influence was gradually diminishing in
333 southern Shandong due to the obstruction of Mount Tai. Spatial heterogeneity within
334 intra-urban areas was further investigated to identify the hotspots of pollution sources.
335 The satellite images in even-numbered rows of **Figure 4** illustrate the spatial disparities
336 of three pollutants around four typical emission sources: thermal power plants,
337 industrial parks, overpasses, and parks. As depicted, these anthropogenic emission
338 sources contribute to higher pollution levels, while the mountain in the park mitigates
339 primary pollution but also increases O₃ concentrations. Industrial sources emit a large
340 number of NO_x and PM_{2.5}, leading to increased pollution of these species compared
341 with other urban microenvironments, which in turn promotes O₃ formation, particularly
342 in downwind areas (Miller et al., 1978; Tang et al., 2020). Although the spatial gradients

343 of pollutants on the street are not as apparent as in the dataset with 100 m resolution
344 (Huang et al., 2021), the predicted spatial variation between various geographical
345 scenes is in satisfactory agreement given the 500 m scale of the model. Urban areas
346 affected by diverse dust pollution exhibit lower PM_{2.5} concentrations compared to rural
347 due to the obstructive and filtering effects of artificial structures, such as buildings and
348 urban greenery (Figure [S10](#)), which cannot be effectively captured solely by ground-
349 based observations. Notably, the elevated PM_{2.5} inhibits the formation of O₃ by
350 diminishing solar radiation flux and absorbing the HO₂ radical on the aerosol surface,
351 even in conditions characterized by similar NO₂ levels. As [for](#) the mapping, AiT
352 accurately grasps the spatial [characteristics](#) of air pollutants and delivers a coherent
353 spatial-temporal distribution that is consistent with the prior knowledge of atmospheric
354 transport.



355

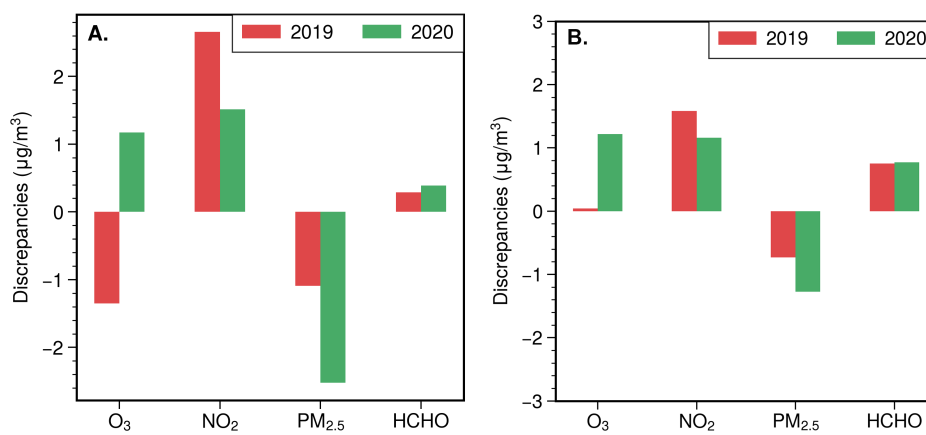
356 **Figure 4.** The spatial distribution of ground-level O₃ (A-D), NO₂ (I-L), and PM_{2.5} (Q-
 357 T) concentrations from AiT and monitoring stations during 13-16 March 2021 in
 358 Shandong, China. The black arrows are the 10 m wind speed and wind direction. The
 359 even-numbered rows correspond to the concentration distribution maps of typical
 360 emission sources for the respective pollutants, accompanied by satellite images (©
 361 Tianditu: www.tianditu.gov.cn). The upper right area of E, M, and U is a thermal power
 362 plant in Weifang City (119° 250' E-119° 280' E, 36° 658' N-36° 673' N). The
 363 center area of F, N, and V is an industrial park in Zibo city (117° 725' E-117° 845'
 364 E, 36° 880' N-36° 940' N). The center and upper right area of G, O, and W is an
 365 overpass and Wanling mountain in Jinan city (116° 977' E-117° 009' E, 36° 590'
 366 N-36° 606' N). The center area of H, P, and X is another overpass in Jinan city (116°
 367 970' E-117° 030' E, 36° 580' N-36° 610' N).

368 3.2 Urban-nonurban Difference

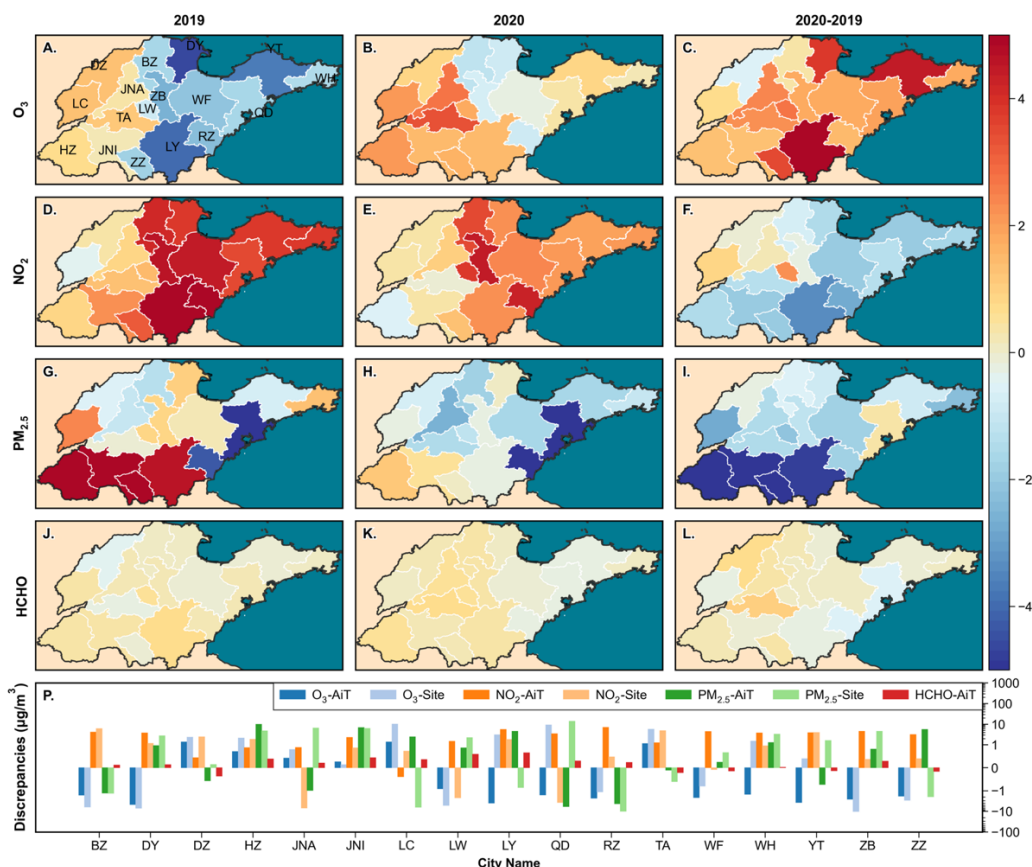
369 Full-coverage pollutant estimates provide a foundational basis for assessing urban-
 370 nonurban disparities, addressing the critical issue of imbalanced site numbers between
 371 urban and rural locations. Table S4 shows the concentrations of O₃, NO₂, PM_{2.5}, and

372 HCHO over the urban and nonurban regions, delineated from an annual urban extents
373 dataset (Zhao et al., 2022). The urban extents in Shandong Province in 2019 are
374 depicted in Figure S11. From 2019 to 2020, surface air pollutant levels declined
375 significantly in Shandong. The averaged concentration discrepancies of these pollutants
376 between urban and nonurban over February to March (lockdown during COVID-19)
377 and June to October (summertime) are shown in **Figure 5**. Surface concentrations of
378 NO₂ and HCHO are higher in urban than nonurban areas, and the differences narrowed
379 from February to October, while PM_{2.5} is the opposite at both. Ground-level O₃ levels
380 exhibited unexpected urban-nonurban disparity variations, from the lockdown period
381 through the summer, as well as from 2019 to 2020. Compared to nonurban areas, the
382 urban areas, which previously had lower O₃ levels, began to experience higher
383 concentrations, attributed to a more rapid decline of ozone in nonurban regions. **Figure**
384 **6** revealed that urban-nonurban differences in O₃ and PM_{2.5} varied across various cities
385 during the lockdown period in 2019, while the higher NO₂ pollution in urban areas
386 remained consistent. In summer, only a handful of urban areas exhibit lower levels of
387 ozone concentration, where NO₂ and PM_{2.5} levels surpass those in nonurban regions,
388 attributable to a more pronounced titration effect of NO and a slower rate of
389 photochemistry reactions (Figure S12) (Sicard et al., 2016, 2020; Zhang et al., 2004).
390 Comparative urban-nonurban differences from 2019 to 2020 indicate an accelerated
391 reduction of ozone and HCHO in non-urban areas, while NO₂ and PM_{2.5} levels in urban
392 have seen a more significant decrease due to the decline in anthropogenic activities,

393 particularly the suspension of emissions from pollution sources located in urban areas.
394 Upon comparing the results of urban-nonurban disparities of our data with monitoring
395 data and the CHAP dataset, we have identified potential overestimations or
396 underestimations across various cities in monitoring data, likely resulting from the
397 limited number of non-urban sites (**Figure 6P, S13**). The notable disparity between the
398 number of urban and non-urban sites in cities such as JNA, LC, LY, QD, and YT results
399 in a pattern of urban-nonurban differences that contrasts markedly with the observed in
400 AiT (Table S5). The urban-nonurban difference calculated by the CHAP generally
401 aligns with our findings (Figure S14). Nevertheless, it is worth noting that the coarse
402 resolution of O₃ (10 km) has led to a significant overestimation. These results highlight
403 the invaluable of high-resolution and gapless data for studying urban-nonurban
404 disparities.



405
406 **Figure 5.** The discrepancies of O₃, NO₂, and PM_{2.5} between urban and non-urban from
407 2019 to 2020 for the lockdown period (A) and summertime (B) averaged concentration.



408

409 **Figure 6.** The urban-nonurban disparities of O₃, NO₂, PM_{2.5} and HCHO calculated by
 410 AiT across cities with administrative divisions in Shandong, China during lockdown
 411 periods in 2019 (A, D, G, J) and 2020 (B, E, H, K), and the changes of differences
 412 between 2019 and 2020 (C, F, I, L). P is the comparison between the results of
 413 monitoring station data and the AiT dataset in 2019. The red color represents a greater
 414 decline in air pollutants in nonurban areas, while the blue color indicates a more
 415 significant reduction in urban areas in the third column of the figure. (YT: Yantai, BZ:
 416 Binzhou, DY: Dongying, WH: Weihai, DZ: Dezhou, JNA: Jinan, QD: Qingdao, WF:
 417 Weifang, ZB: Zibo, LC: Liaocheng, LW: Laiwu, TA: Taian, LY: Linyi, RZ: Rizhao, JNI:
 418 Jining, HZ: Hezhe, ZZ: Zaozhuang)

419 3.3 Photochemical Regimes

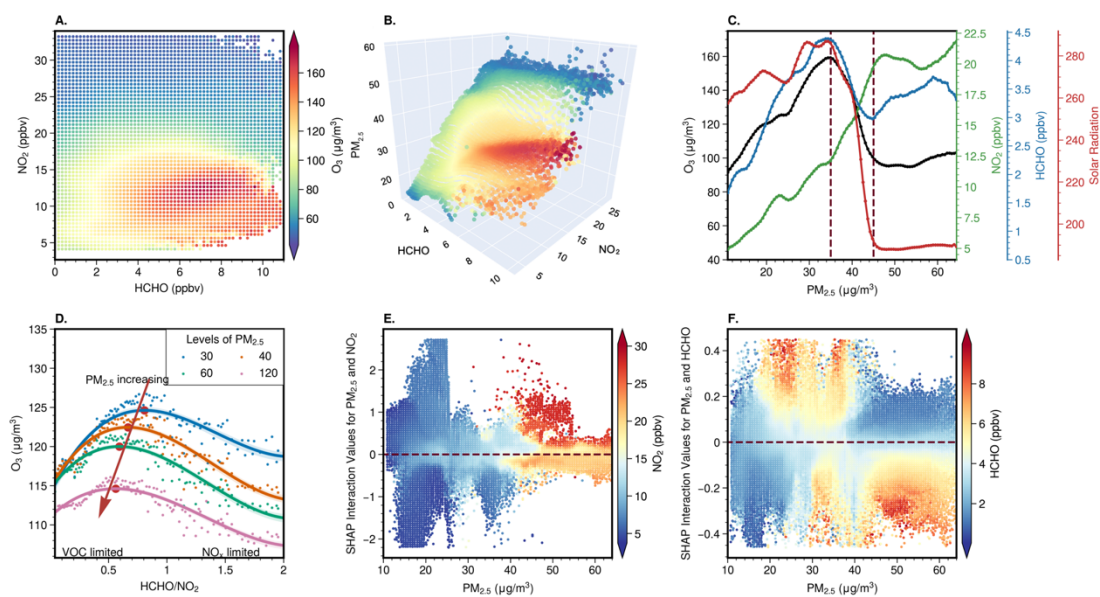
420 3.3.1 Ozone-NO_x-VOCs-Aerosols Sensitivity

421 Figure S15 shows the seasonal maps of O₃, PM_{2.5}, and NO₂ estimations from AiT,
 422 and satellite-derived surface HCHO. Based on these data, we first capture the well-
 423 established non-linearities in O₃-VOC-NO_x chemistry by a conceptual framework

424 similar to classic O₃ isopleths typically generated with models (Pusede et al., 2015; Ren
425 et al., 2022a). **Figure 7A** depicts O₃ concentration as a function of HCHO and NO₂,
426 which was derived solely from ground-level estimation. The result indicates that the O₃
427 regimes can be qualitatively identified based on the nonlinear interaction between
428 surface O₃, HCHO, and NO₂. In the regime characterized by high NO₂ and low HCHO,
429 the elevated consumption of HO_x, predominantly driven by the OH + NO₂ termination
430 reaction, results in the suppression of NO_x on O₃, indicating the prevalence of VOC-
431 limited chemistry. Conversely, when HCHO levels are high and NO₂ levels are
432 relatively low, O₃ increases with NO₂ and exhibits insensitivity to HCHO due to
433 abundant peroxy radicals (HO₂ + organic peroxy (RO₂) radicals, RO_x) self-reactions,
434 suggesting NO_x-limited (VOC-saturated) chemistry. In cases where high HCHO and
435 NO₂, the O₃ increases with both HCHO and NO₂, reaching a peak. While **Figure 7A**
436 resembles this overall O₃-VOC-NO_x, the blurry transition between two different
437 regimes and the role of PM_{2.5} is uncertain which may be influenced by meteorological
438 conditions, chemical and depositional loss of O₃, errors of estimations, and “aerosol-
439 inhibited”. Increasing PM_{2.5} levels could suppress O₃ formation even under high HCHO
440 and NO₂ conditions (**Figure 7B**), which could be induced by enhanced reactive uptake
441 of HO₂ onto aerosol particles and weaker photochemical reaction resulting from the
442 scattering and absorption of solar radiation by anthropogenic aerosols. The relationship
443 between PM_{2.5} and O₃ in Shandong demonstrates the distinct stages of O₃ chemistry, as
444 depicted in **Figure 7C**. When PM_{2.5} was below the maximum turning point (MTP1, 35

445 $\mu\text{g}/\text{m}^3$), a linear and positive correlation between O_3 and $\text{PM}_{2.5}$ was observed due to the
446 common dependence on precursors in the initial stage (Zhang et al., 2022). As $\text{PM}_{2.5}$
447 increased beyond the MTP1, a sharp reduction in HCHO and O_3 was observed,
448 accompanied by a decline in surface short-wave radiation, reflecting their formation as
449 photo-oxidation products of OVOCs and NO_x . When $\text{PM}_{2.5}$ exceeded the minimum
450 transition point (MTP2, $45 \mu\text{g}/\text{m}^3$), a phase was observed with stagnant radiation
451 intensity and relatively higher NO_2 levels compared to HCHO. This regime is typically
452 associated with a VOC-limited regime, where an increase in HCHO and a decrease in
453 NO_2 concentration could promote O_3 production. However, our findings demonstrated
454 an opposite impact of HCHO and NO_2 on O_3 when $\text{PM}_{2.5}$ exceeded MTP2. **Figure 7D**
455 shows the changes in the quantitative relationships between HCHO/ NO_2 (FNR) and O_3
456 by artificially changing $\text{PM}_{2.5}$ and precursors levels for XGBoost, in which the peak of
457 curves marks the transitional threshold of O_3 regimes from VOC to NO_x sensitive. It
458 can be seen that attenuated $\text{PM}_{2.5}$ pollution could increase the sensitivity of O_3 to VOCs
459 and decrease the sensitivity to NO_x , which causes the shift in O_3 regimes from NO_x -
460 limited to VOC-limited. With the recent reduction in NO_x emissions in China, the
461 anticipated transition of the O_3 production regime in urban areas towards being more
462 NO_x -limited has been impeded by the heightened VOC sensitivity resulting from
463 decreased $\text{PM}_{2.5}$ levels. Our results are consistent with the findings of Li et al. regrading
464 O_x - NO_x relationship in response to changing $\text{PM}_{2.5}$ (Li et al., 2022a), and with the
465 findings of Dyson et al. on the impact of HO_2 aerosol uptake on O_3 production (Dyson

466 et al., 2023). The SHAP interaction plots in Figures 7E and F illustrate that the
467 influence of NO₂ and HCHO on O₃ formation is not constant and is influenced by the
468 levels of PM_{2.5}. Typically, at a certain level of PM_{2.5}, a lower NO concentration results
469 in a stronger inhibitory effect on O₃ production. This could be due to aerosols exerting
470 stronger suppression through the HO₂ sink at lower NO_x levels. As the concentration of
471 PM_{2.5} increases, often accompanied by a concurrent increase in NO₂ as a key precursor,
472 there is a greater need for higher levels of NO₂ to be converted into nitrous acid (HONO)
473 through the heterogeneous uptake by aerosols. This process produces more OH radicals,
474 which facilitate photochemical O₃ formation, thereby offsetting the increased inhibitory
475 effect of the HO₂ sink. Under high PM_{2.5} concentrations, an increase in NO₂ along with
476 a decrease in HCHO enhances their effect on promoting O₃ formation. This
477 enhancement could be caused by increased titration of O₃ by NO_x resulting from weaker
478 conversion of NO to NO_x through the RO_x radical. Meanwhile, the impact of HCHO
479 shifts from promoting to suppressing as PM_{2.5} pollution intensifies. It further illustrates
480 that the scavenging of HO₂ on aerosols can cause the shift in O₃ regimes from being
481 VOC-limited to NO_x-limited and the threshold approach is restricted by aerosols and
482 meteorology for determining the constantly changing O₃ formation regimes over time
483 and space.



484

485 **Figure 7.** (A) O₃ concentrations as a function of surface HCHO and NO₂. (B) O₃
 486 concentrations as a function of surface HCHO, NO₂, and PM_{2.5}. Both A and B utilize a
 487 shared color bar to indicate O₃ concentrations, enhancing comparability. (C)
 488 Relationship between O₃, and NO₂, HCHO₂ and surface short-wave radiation flux. The
 489 paired O₃, HCHO, NO₂ and solar radiation are divided into 100 bins based on PM_{2.5}
 490 and then the averaged concentrations (y-axis) are calculated for each PM_{2.5} bin (x-axis).
 491 (D) Changes in HCHO/NO₂-O₃ relationship in response to changing PM_{2.5} by XGBoost
 492 model. The solid lines are fitted with four-order polynomial curves, and the shading
 493 indicates 95% confidence intervals. (E-F) The interaction SHAP values reveal an
 494 interesting hidden relationship between pairwise variables (PM_{2.5} and NO₂, HCHO) and
 495 O₃.

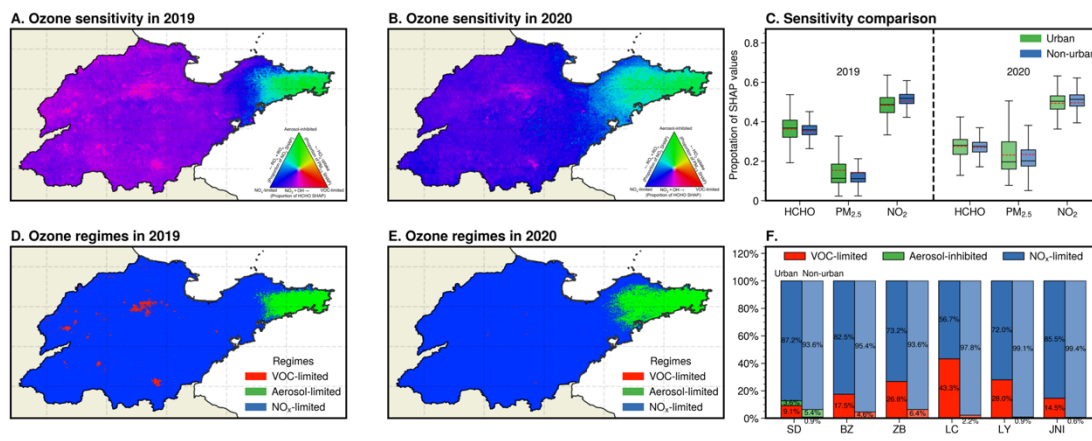
496 Unraveling the intricate interplay of O₃ with meteorology, aerosols, and precursors
 497 that govern O₃ formation over extensive spatial domains has long confounded robust
 498 interpretation. These multiscale processes were elucidated using an interpretable ML
 499 model, which can quantify the positive or negative contributions of individual processes.

500 As depicted in Figure S16, the performance of the XGBoost model is robust, evidenced
 501 by a high R² value of 0.99 coupled with a low RMSE of 3.24 μg/m³ and MAE of 2.33

502 μg/m³. Figure S17 elucidates that meteorological variations, chiefly surface short-wave

503 radiation flux modulating photochemical reaction kinetics, primarily dictate the

504 heterogeneous geographic distribution of O₃ at the regional scale, with lower levels
505 over [the](#) Jiaodong Peninsula. Meanwhile, local atmospheric chemical processes
506 predominate the city-scale variability of O₃. HCHO facilitated O₃ formation in urban
507 areas yet suppressed it in rural regions across areas with high ozone, where most NO₂
508 promoted O₃ production overall, indicating VOC-NO_x synergistic control on O₃ in cities
509 and a NO_x-limited regime in rural areas during summertime. The contribution of NO₂
510 and PM_{2.5} exhibits analogous seasonal variability, promoting O₃ formation under low
511 pollution conditions while inhibiting O₃ when pollution levels are high ([Figures S15](#)
512 [and 18](#)). The elevated NO₂ levels in autumn led to a negative contribution to O₃,
513 whereas the facilitating effect of PM_{2.5} was enhanced. This stems from the relatively
514 moderate PM_{2.5} concentrations slightly affecting photochemical reaction rates, while
515 the increased NO₂ amplified the reactive uptake of NO₂ by PM_{2.5}, generating more OH
516 radicals that promote O₃ formation (Lin et al., 2023; Tan et al., 2022). In winter, PM_{2.5}
517 pollution exceeding 75 μg/m³ suppressed O₃ formation through scattering and
518 absorbing solar radiation that activates atmospheric chemical processes, which
519 counteracted the promoting effect of high PM_{2.5} through the conversion of NO₂ to
520 HONO.



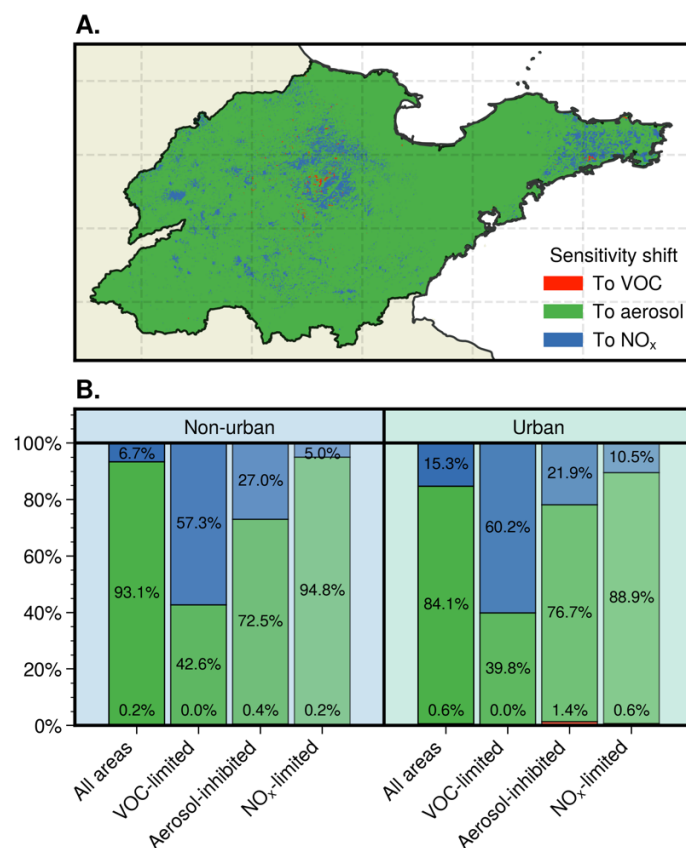
521

522 **Figure 8.** Comparison of geographical distribution for ozone formation regimes
 523 between 2019 and 2020 in the summertime. All surface daily O₃, PM_{2.5}, and NO₂
 524 estimations from Air Transformer (AiT) are averaged over each month from May to
 525 October 2019-2020 for matching monthly HCHO derived from TROPOMI (500 * 500
 526 m). (A, B) Geographical distribution of fractional contribution of chemical factors
 527 representing O₃ formation regimes. The ternary phase diagram in the legend depicts the
 528 normalized fraction of SHAP values for O₃ attributed to HCHO, NO₂, and PM_{2.5} at the
 529 surface, representing VOC-limited (red), aerosol-inhibited (green), and NO_x-limited
 530 (blue) regimes, respectively. (C) Statistical Changes in the fractional contribution of
 531 chemical factors. (D, E) Geographical distribution of O₃ chemical regimes. (F)
 532 Proportion of three O₃ chemical regimes across urban and nonurban areas in 2019 in
 533 Shandong (SD), and individual cities (BZ: Binzhou, ZB: Zibo, LC: Liaocheng, LY:
 534 Linyi, JNI: Jining).

535 **Figure 8A-C** shows surface distribution and changes of the relative proportions of
 536 SHAP values on three pollutants for inferring O₃ photochemical regimes. Moving along
 537 an urban-to-rural gradient, reactions dominated by RO_x radical self-reactions are
 538 continuously enhanced with increasing NO_x SHAP values, resulting in the majority of
 539 rural Shandong being situated in NO_x-limited regimes. Furthermore, the overall ozone
 540 production regimes in Shandong exhibited a transition toward more NO_x-limited from
 541 2019 to 2020, with regions dominated by NO_x-limited shifting toward being aerosol-
 542 inhibited in the Jiaodong Peninsula. The aerosol-inhibited regime differs from either of

543 the two classically applied tropospheric O₃ policy-control regimes. It is attributed to the
544 predominant heterogeneous HO₂ uptake by aqueous aerosols, despite comparatively
545 low PM_{2.5} levels during summertime. The marine environment engenders liquid aerosol
546 particles with HO₂ uptake coefficients exceeding those of dry aerosols by orders of
547 magnitude (Song et al., 2022a). Concurrently, lower ambient NO_x levels minimize the
548 promotive effects of aerosols on ozone formation (Tan et al., 2022; Kohno et al., 2022).
549 This result is consistent with the findings of Dyson et al. (Dyson et al., 2023), which
550 concluded that the contribution of HO₂ sinks onto aerosols on total HO₂ could increase
551 for areas with low NO levels. The attenuated responsiveness of O₃ formation to VOCs
552 induced by the uptake of HO₂ results in enhanced sensitivity of NO_x at the northwest
553 boundary region of the Jiaodong Peninsula. Collectively, these processes delineate an
554 aerosol-inhibited ozone production regime in this coastal region, reflecting the
555 sensitivity of O₃ photochemistry to the HO₂ sink. In several cities, including Binzhou,
556 Zibo, Liaocheng, Linyi, and Jining, a greater proportion of urban areas, as compared to
557 their nonurban counterparts, exhibited a VOC-limited regime in 2019, as indicated by
558 the prevalence of red regions in Figure 8D. The percentage of urban areas in these cities
559 under a VOC-limited regime ranges from 15% to 43%, in stark contrast to non-urban
560 areas where such a regime is typically rare (Figure 8F). The comparison of O₃
561 sensitivities from 2019 to 2020 shows a regional shift towards increased sensitivity to
562 aerosol and NO_x, along with a decreased VOC sensitivity as a result of NO_x reduction
563 (Figure 8A-C). This shift has led to the majority of areas in Shandong being dominated

564 by a NO_x-limited regime in 2020, with an expanded aerosol-inhibited regime region in
 565 the Jiaodong Peninsula (Figure 8E). Additionally, the discrepancy in O₃ formation
 566 sensitivity between urban and non-urban areas has been diminishing during this period
 567 (Figure 8C). As illustrated in Figure 9, while the ozone regime transitions towards
 568 NO_x-limited, there is a marked shift towards greater aerosol sensitivity across nearly
 569 90% of areas, leading to a 1.6% increase in aerosol-inhibited grids. Compared to
 570 nonurban regions, a higher number of grids in urban areas demonstrate a shift towards
 571 NO_x sensitivity. Conversely, urban areas that were predominantly aerosol-inhibited in
 572 2019 showed a lower sensitivity shift towards NO_x.

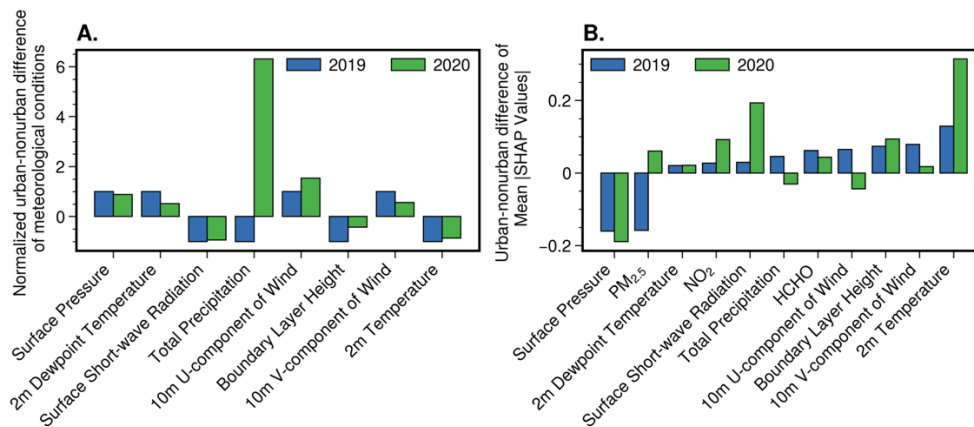


573
 574 **Figure 9.** Geographical distribution of changes in ozone sensitivity from 2019 to 2020
 575 in summertime (A). Comparison of ozone sensitivity changes across areas dominated
 576 by different chemical regimes in 2019 between urban and non-urban areas (B).

3.3.2 Impact on Urban-nonurban Differences

We further explore the reversed O₃ differences by separating the individual contributions of climate and anthropogenic changes using an interpretable machine learning model (Figure 10). The results demonstrate that atmospheric chemical processes and meteorological conditions commonly dominate the discrepancies in O₃ levels between urban and non-urban areas. From 2019 to 2020, meteorological shifts remained uniform across urban and non-urban regions, marked by lowered surface pressure, boundary layer height, and short-wave radiation, alongside heightened precipitation. This, coupled with decreased precursor levels, contributed to a decline in O₃ pollution. As shown in Figures 10 and S19, the diminished reduction in boundary layer height and radiation flux across urban areas, compared to nonurban areas in 2020, decelerated the expected decline of O₃ concentrations, leading to urban O₃ levels exceeding those of nonurban areas. Concurrently, a narrowing difference in temperatures between urban and nonurban areas, despite an overall cooling from 2019 to 2020, favored O₃ formation in urban regions during the summertime. Additionally, PM_{2.5} emerged as the principal anthropogenic factor inverting the urban-nonurban O₃ disparity over the course of 2019 to 2020. Its contribution to ozone shifted from being lower in urban areas to exceeding that in nonurban areas, revealing that the decreased reactive uptake of HO₂ from aerosols induced by a more substantial reduction in PM_{2.5} in urban areas made the larger contribution to O₃ production (Ivatt et al., 2022; Li et al., 2017). Moreover, the response of O₃ to the changes in its precursors and PM_{2.5} was

608 determined by the O_3 formation regimes. The variations in O_3 sensitivity also
 609 corroborate the above finding. In rural areas, where there was a lesser reduction in $PM_{2.5}$
 610 concentration, the sensitivity increasingly favored aerosol suppression across more than
 611 93% of the assessed grids (Figure 9). This enhanced suppression effect of aerosols in
 612 rural areas leads to a more significant O_3 reduction compared to urban locales. The
 613 reduction of NO_x in nonurban areas demonstrated a more effective reduction in O_3
 levels, which predominantly shifted towards a NO_x -limited regime in 2020. Although
 urban areas also showed a shift towards being a NO_x -limited regime, they exhibited
 relatively higher sensitivity to VOCs (Figure 8). The urban areas, characterized by
 elevated NO_x emissions, exhibited a higher sensitivity to VOCs, and the fraction of
 aerosol-inhibited areas increased from 2019 to 2020, resulting in the control benefits of
 urban O_3 pollution in 2020 are partially offset by the nonlinear response of O_3 to a
 greater reduction in NO_2 and $PM_{2.5}$, and a smaller decrease in HCHO relative to
 nonurban areas. Consequently, O_3 exhibits a lower reduction in urban areas as a result
 of the aforementioned changes.



614 **Figure 10.** Comparison of urban-nonurban disparities in meteorological conditions (A),
615 and mean absolute SHAP values (B) between 2019 and 2020 across Shandong, China
616 during the summertime.

617 4. CONCLUSIONS

618 The purpose of the current study was to diagnose the non-linearity of O₃-NO_x-
619 VOCs-aerosols chemistry using an interpretable ML model based on spatially resolved
620 multi-pollutant estimations for determining the causes of changing differences in O₃
621 levels between urban and non-urban areas. Our study represents the first attempt to
622 develop an advanced DL model that reconstructs the concentrations of multiple
623 pollutants and subsequently infers the aerosol-inhibited regime from observations. This
624 innovative approach provides further support for investigating the impact of precursor
625 emissions and aerosol on the urban-nonurban differences in O₃ levels.

626 Given the non-linearity of ozone formation and its increasing regional differences,
627 precise estimations of ground-level O₃, NO₂, HCHO, and PM_{2.5} are crucial for deducing
628 the chemical regimes governing ozone pollution and its urban-nonurban disparities. The
629 evaluation of the model's performance indicates that it can be readily extended to any
630 other domain thanks to its unified architecture. Anyone can easily utilize the model to
631 estimate ground-level pollutants, intelligently considering spatial-temporal
632 neighborhood information based on their customized input data. The model further
633 improved spatial resolution to sub-km levels using TROPOMI and MODIS retrievals
634 via spatiotemporal autocorrelation downscaling of AiT. The "black box" nature of AiT
635 can be made more physically interpretable by SHAP, enabling the evaluation of the

636 significance of each input variable (Figure S20). The season trends show the highest
637 contribution, followed by emission proxies and meteorological conditions. Meanwhile,
638 the results between AiT trained with all data and that trained exclusively with CNEMC
639 data across various spatiotemporal scales underscore the promising prospect for
640 improving the model's generalization ability with more ground-level monitoring data
641 and the growing space of methods.

642 We conclude that with the effective reduction of PM_{2.5} pollution, the sensitivity of
643 O₃ to VOCs will increase, necessitating further intensification of VOC emissions
644 regulation by government agencies. Three distinct chemical regimes were assessed by
645 tracking NO_x, VOCs, and aerosols with surface NO₂, HCHO, and PM_{2.5}. In the
646 Jiaodong Peninsula of Shandong Province, coastal areas with relatively few primary
647 pollutants are widely found to be under an aerosol suppression regime, illustrating that
648 ozone regime inference based on machine learning can serve as an alternative to
649 determining the aerosol suppression regime through the rate of radical termination in
650 atmospheric chemical models. The O₃ regime in other areas of Shandong generally
651 transited from the NO_x-sensitive regime in nonurban to a more VOC-sensitive regime
652 in urban areas. We estimate that substantial reductions in anthropogenic emissions of
653 PM_{2.5} and NO₂ are the main drivers of the reversal of the traditional discrepancy in O₃
654 levels between urban and non-urban areas. In essence, due to the lower efforts in
655 reducing PM_{2.5} in nonurban settings, the aerosol-mediated suppression of ozone
656 became more pronounced, resulting in lower ozone levels in rural areas relative to urban

657 centers. This shift underlines the intricate balance between emission reduction and
658 ozone formation mechanisms, suggesting that nuanced understanding and targeted
659 interventions are necessary to manage and mitigate the health and environmental
660 impacts of such disparities. To preclude exacerbated O₃ pollution resulting from the
661 shift of many regions from VOC-limited to NO_x-limited regimes and the decline in
662 heterogeneous HO₂ uptake induced by PM_{2.5} reduction in urban areas, emission policies
663 aimed at decreasing NO_x to reduce O₃ levels will only be effective with stringent VOC
664 emission abatement when PM_{2.5} is concurrently decreased. The integration of high-
665 resolution pollutant estimations with an interpretable machine learning model offers a
666 promising avenue for advancing our understanding of ozone pollution dynamics and
667 developing effective air quality management strategies.

668 ~~The season trends show the highest contribution, followed by emission proxies~~
669 ~~and meteorological conditions.~~ Although our study endeavors to establish O₃ formation
670 regimes involving NO_x, VOCs, and aerosols, and the method identifies an aerosol-
671 inhibited regime from a statistical perspective, it is subject to certain uncertainties due
672 to the relatively poor data quality of HCHO and the unsegregated multiple impacts of
673 aerosols, such as N₂O₅ uptake, NO₂ uptake, HO₂ uptake, and light extinction (Tan et
674 al., 2022). We have made efforts to integrate all required surface pollutant
675 concentrations into a unified model, while the absence of ground-level HCHO
676 monitoring data compelled us to tap into an alternative methodology. The retrieval error
677 of surface HCHO and the system error between its retrieval approach and the AiT model

678 degrade the ability of ML to identify the O₃ sensitivity. Meanwhile, the notion of ozone
679 regimes is only appreciated in photochemically active environments where the RO_x-
680 HO_x cycle is active (Souri et al., 2023). The definition of NO_x-limited or VOC-limited
681 regimes is meaningless in nighttime chemistry, where NO-O₃-NO₂ partitioning is the
682 primary driver. The surface daytime pollutant estimations with finer resolutions in
683 space and time based on a unified modeling framework will offer an unprecedented
684 view to characterize the near-surface O₃ formation regimes. Notwithstanding the
685 relatively limited duration of the study, this work offers valuable insights into the
686 current state and causes of urban-nonurban disparities in O₃ pollution. Future efforts
687 should conduct a more detailed long-term evaluation of urban-nonurban disparities in
688 global O₃ levels and the impact of formation mechanisms to further our understanding
689 of air pollution and its mitigation.

690 **Competing Interests**

691 The authors declare that they have no conflict of interest.

692 **Acknowledgments**

693 The work was financially supported by the National Natural Science Foundation
694 of China (project No. 22236004) and Taishan Scholars (No. ts201712003).

695 **Code and Data Availability**

696 The Air Transformer deep learning framework is available on GitHub
697 (<https://github.com/myles-tcl/Air-Transformer>), which provides the scripts for
698 spatiotemporal data extraction, normalization, model training, and estimating of multi-

699 pollutants. The sources of input data in the Air Transformer can be found in Table S1.
700 The estimation of the Air Transformer can be downloaded from Zenodo:
701 <https://zenodo.org/records/10071408> (Tao, 2023).

702 **Author Contributions**

703 CT: Methodology, Software, Validation, Formal analysis, Investigation, Data
704 Curation, Writing-Original Draft, Visualization. YP: Conceptualization, Writing-
705 Review & Editing. QZ: Writing-Review & Editing, Project administration, Funding
706 acquisition. YZ: Methodology, Writing-Review & Editing. BG: Software, Writing-
707 Review & Editing. QW: Supervision, Writing-Review & Editing. WW: Supervision,
708 Writing-Review & Editing.

709

710 **References**

- 711 Bertasius, G., Wang, H., and Torresani, L.: Is Space-Time Attention All You Need for
712 Video Understanding?, <http://arxiv.org/abs/2102.05095>, 9 June 2021.
- 713 Chen, T. and Guestrin, C.: XGBoost: A Scalable Tree Boosting System, in: Proceedings
714 of the 22nd ACM SIGKDD International Conference on Knowledge Discovery
715 and Data Mining, KDD'16: The 22nd ACM SIGKDD International Conference
716 on Knowledge Discovery and Data Mining, San Francisco California USA, 785–
717 794, <https://doi.org/10/gdp84q>, 2016.
- 718 Action Plan on Air Pollution Prevention and Control (in Chinese):
719 http://www.gov.cn/zwggk/2013-09/12/content_2486773.htm, last access: 1
720 February 2023.
- 721 Chu, W., Li, H., Ji, Y., Zhang, X., Xue, L., Gao, J., and An, C.: Research on ozone
722 formation sensitivity based on observational methods: Development history,
723 methodology, and application and prospects in China, *Journal of Environmental*
724 *Sciences*, S1001074223000980, <https://doi.org/10/gr4qzk>, 2023.
- 725 Cooper, M. J., Martin, R. V., Hammer, M. S., Levelt, P. F., Veefkind, P., Lamsal, L. N.,
726 Krotkov, N. A., Brook, J. R., and McLinden, C. A.: Global fine-scale changes in
727 ambient NO₂ during COVID-19 lockdowns, *Nature*, 601, 380–387,
728 <https://doi.org/10.1038/s41586-021-04229-0>, 2022.
- 729 Copernicus Sentinel-5P (processed by ESA): TROPOMI Level 2 Ozone Total Column
730 products (Version 02), <https://doi.org/10.5270/S5P-ft13p57>, 2020.
- 731 Di, Q., Kloog, I., Koutrakis, P., Lyapustin, A., Wang, Y., and Schwartz, J.: Assessing
732 PM_{2.5} Exposures with High Spatiotemporal Resolution across the Continental
733 United States, *Environ. Sci. Technol.*, 50, 4712–4721,
734 <https://doi.org/10.1021/acs.est.5b06121>, 2016.
- 735 Dias, D. and Tchepel, O.: Spatial and Temporal Dynamics in Air Pollution Exposure
736 Assessment, *IJERPH*, 15, 558, <https://doi.org/10.3390/ijerph15030558>, 2018.
- 737 Didan, K.: MODIS/Terra Vegetation Indices 16-Day L3 Global 250m SIN Grid V061,

738 NASA EOSDIS Land Processes Distributed Active Archive Center,
739 <https://doi.org/10.5067/MODIS/MOD13Q1.061>, 2021.

740 van Donkelaar, A., Martin, R. V., Spurr, R. J. D., and Burnett, R. T.: High-Resolution
741 Satellite-Derived PM_{2.5} from Optimal Estimation and Geographically Weighted
742 Regression over North America, *Environ. Sci. Technol.*, 49, 10482–10491,
743 <https://doi.org/10.1021/acs.est.5b02076>, 2015.

744 Dosovitskiy, A., Beyer, L., Kolesnikov, A., Weissenborn, D., Zhai, X., Unterthiner, T.,
745 Dehghani, M., Minderer, M., Heigold, G., Gelly, S., Uszkoreit, J., and Housby,
746 N.: An Image is Worth 16x16 Words: Transformers for Image Recognition at Scale,
747 <https://doi.org/10.48550/arXiv.2010.11929>, 3 June 2021.

748 Dyson, J. E., Whalley, L. K., Slater, E. J., Woodward-Massey, R., Ye, C., Lee, J. D.,
749 Squires, F., Hopkins, J. R., Dunmore, R. E., Shaw, M., Hamilton, J. F., Lewis, A.
750 C., Worrall, S. D., Bacak, A., Mehra, A., Bannan, T. J., Coe, H., Percival, C. J.,
751 Ouyang, B., Hewitt, C. N., Jones, R. L., Crilley, L. R., Kramer, L. J., Acton, W. J.
752 F., Bloss, W. J., Saksakulkrai, S., Xu, J., Shi, Z., Harrison, R. M., Kotthaus, S.,
753 Grimmond, S., Sun, Y., Xu, W., Yue, S., Wei, L., Fu, P., Wang, X., Arnold, S. R.,
754 and Heard, D. E.: Impact of HO₂ aerosol uptake on radical levels and O₃
755 production during summertime in Beijing, *Atmos. Chem. Phys.*, 23, 5679–5697,
756 <https://doi.org/10/gshrst>, 2023.

757 Geng, G., Xiao, Q., Liu, S., Liu, X., Cheng, J., Zheng, Y., Xue, T., Tong, D., Zheng, B.,
758 Peng, Y., Huang, X., He, K., and Zhang, Q.: Tracking Air Pollution in China: Near
759 Real-Time PM_{2.5} Retrievals from Multisource Data Fusion, *Environ. Sci. Technol.*,
760 55, 12106–12115, <https://doi.org/10.1021/acs.est.1c01863>, 2021.

761 Global Modeling and Assimilation Office (GMAO): MERRA-2 inst3_2d_gas_Nx: 2d,
762 3-Hourly, Instantaneous, Single-Level, Assimilation, Aerosol Optical Depth
763 Analysis V5.12.4, Greenbelt, MD, USA, Goddard Earth Sciences Data and
764 Information Services Center (GES DISC),
765 <https://doi.org/10.5067/HNGA0EWW0R09>, 2015.

766 Han, H., Zhang, L., Liu, Z., Yue, X., Shu, L., Wang, X., and Zhang, Y.: Narrowing
767 Differences in Urban and Nonurban Surface Ozone in the Northern Hemisphere
768 Over 1990–2020, *Environ. Sci. Technol. Lett.*, 10, 410–417,
769 <https://doi.org/10/gsd5gk>, 2023.

770 Han, X. and Naeher, L. P.: A review of traffic-related air pollution exposure assessment
771 studies in the developing world, *Environment International*, 32, 106–120,
772 <https://doi.org/10.1016/j.envint.2005.05.020>, 2006.

773 Hersbach, H., Bell, B., Berrisford, G., Horányi, A., Muñoz Sabater, J., Nicolas, J.,
774 Peubey, C., Rozum, I., Schepers, D., Simmons, A., Soci, C., Dee, D., and Thépaut,
775 J.-N.: ERA5 hourly data on single levels from 1959 to present, Copernicus Climate
776 Change Service (C3S) Climate Data Store (CDS),
777 <https://doi.org/10.24381/cds.adbb2d47>, 2023.

778 Huang, C., Hu, J., Xue, T., Xu, H., and Wang, M.: High-Resolution Spatiotemporal
779 Modeling for Ambient PM_{2.5} Exposure Assessment in China from 2013 to 2019,
780 *Environ. Sci. Technol.*, 55, 2152–2162, <https://doi.org/10.1021/acs.est.0c05815>,
781 2021.

782 Inness, A., Ades, M., Agustí-Panareda, A., Barré, J., Benedictow, A., Blechschmidt, A.-
783 M., Dominguez, J. J., Engelen, R., Eskes, H., Flemming, J., Huijnen, V., Jones, L.,
784 Kipling, Z., Massart, S., Parrington, M., Peuch, V.-H., Razinger, M., Remy, S.,
785 Schulz, M., and Suttie, M.: The CAMS reanalysis of atmospheric composition,
786 *Atmos. Chem. Phys.*, 19, 3515–3556, <https://doi.org/10/ghdkrm>, 2019.

787 Ivatt, P. D., Evans, M. J., and Lewis, A. C.: Suppression of surface ozone by an aerosol-
788 inhibited photochemical ozone regime, *Nat. Geosci.*, 15, 536–540,
789 <https://doi.org/10.1038/s41561-022-00972-9>, 2022.

790 Jerrett, M., Arain, A., Kanaroglou, P., Beckerman, B., Potoglou, D., Sahsuvaroglu, T.,
791 Morrison, J., and Giovis, C.: A review and evaluation of intraurban air pollution
792 exposure models, *Journal of Exposure Science & Environmental Epidemiology*,
793 15, 185–204, <https://doi.org/10.1038/sj.jea.7500388>, 2005.

794 Jin, X., Fiore, A. M., Murray, L. T., Valin, L. C., Lamsal, L. N., Duncan, B., Folkert
795 Boersma, K., De Smedt, I., Abad, G. G., Chance, K., and Tonnesen, G. S.:
796 Evaluating a Space-Based Indicator of Surface Ozone-NO_x-VOC Sensitivity Over
797 Midlatitude Source Regions and Application to Decadal Trends: Space-Based
798 Indicator of O₃ Sensitivity, *J. Geophys. Res. Atmos.*, 122, 10,439-10,461,
799 <https://doi.org/10.1002/2017JD026720>, 2017.

800 Jin, X., Fiore, A., Boersma, K. F., Smedt, I. D., and Valin, L.: Inferring Changes in
801 Summertime Surface Ozone-NO_x-VOC Chemistry over U.S. Urban Areas from
802 Two Decades of Satellite and Ground-Based Observations, *Environ. Sci. Technol.*,
803 54, 6518–6529, <https://doi.org/10.1021/acs.est.9b07785>, 2020.

804 Jin, X., Fiore, A. M., and Cohen, R. C.: Space-Based Observations of Ozone Precursors
805 within California Wildfire Plumes and the Impacts on Ozone-NO_x-VOC
806 Chemistry, *Environ. Sci. Technol.*, 57, 14648–14660,
807 <https://doi.org/10.1021/acs.est.3c04411>, 2023.

808 Jun, C., Ban, Y., and Li, S.: China: Open access to Earth land-cover map, *Nature*, 514,
809 434–434, <https://doi.org/DOI:10.1038/514434c>, 2014.

810 Jung, J., Choi, Y., Souri, A. H., Mousavinezhad, S., Sayeed, A., and Lee, K.: The Impact
811 of Springtime-Transported Air Pollutants on Local Air Quality With Satellite-
812 Constrained NO_x Emission Adjustments Over East Asia, *Journal of Geophysical*
813 *Research: Atmospheres*, 127, e2021JD035251,
814 <https://doi.org/10.1029/2021JD035251>, 2022.

815 Ke, G., Meng, Q., Finley, T., Wang, T., Chen, W., Ma, W., Ye, Q., and Liu, T.-Y.:
816 LightGBM: A Highly Efficient Gradient Boosting Decision Tree, in: *Proceedings*
817 *of the 31st International Conference on Neural Information Processing Systems*,
818 Red Hook, NY, USA, event-place: Long Beach, California, USA, 3149–3157,
819 2017.

820 Kohno, N., Zhou, J., Li, J., Takemura, M., Ono, N., Sadanaga, Y., Nakashima, Y., Sato,
821 K., Kato, S., Sakamoto, Y., and Kajii, Y.: Impacts of missing OH reactivity and

822 aerosol uptake of HO₂ radicals on tropospheric O₃ production during the AQUAS-
823 Kyoto summer campaign in 2018, *Atmospheric Environment*, 281, 119130,
824 <https://doi.org/10/gshfc4>, 2022.

825 Lamsal, L. N., Krotkov, N. A., Marchenko, S. V., Joiner, J., Oman, L., Vasilkov, A.,
826 Fisher, B., Qin, W., Yang, E.-S., Fasnacht, Z., Choi, S., Leonard, P., and Haffner,
827 D.: TROPOMI/S5P NO₂ Tropospheric, Stratospheric and Total Columns MINDS
828 1-Orbit L2 Swath 5.5 km x 3.5 km, Goddard Earth Sciences Data and Information
829 Services Center (GES DISC),
830 <https://doi.org/10.5067/MEASURES/MINDS/DATA203>, 2022.

831 Lee, H. J., Kuwayama, T., and FitzGibbon, M.: Trends of ambient O₃ levels associated
832 with O₃ precursor gases and meteorology in California: Synergies from ground
833 and satellite observations, *Remote Sensing of Environment*, 284, 113358,
834 <https://doi.org/10.1016/j.rse.2022.113358>, 2023.

835 Li, C., Zhu, Q., Jin, X., and Cohen, R. C.: Elucidating Contributions of Anthropogenic
836 Volatile Organic Compounds and Particulate Matter to Ozone Trends over China,
837 *Environ. Sci. Technol.*, 56, 12906–12916, <https://doi.org/10.1021/acs.est.2c03315>,
838 2022a.

839 Li, D., Wang, S., Xue, R., Zhu, J., Zhang, S., Sun, Z., and Zhou, B.: OMI-observed
840 HCHO in Shanghai, China, during 2010–2019 and ozone sensitivity inferred by
841 an improved HCHO / NO₂ ratio, *Atmos. Chem. Phys.*, 21, 15447–15460,
842 <https://doi.org/10.5194/acp-21-15447-2021>, 2021a.

843 Li, K., Jacob, D. J., Liao, H., Zhu, J., Shah, V., Shen, L., Bates, K. H., Zhang, Q., and
844 Zhai, S.: A two-pollutant strategy for improving ozone and particulate air quality
845 in China, *Nat. Geosci.*, 12, 906–910, <https://doi.org/10.1038/s41561-019-0464-x>,
846 2019.

847 Li, K., Wang, Y., Peng, G., Song, G., Liu, Y., Li, H., and Qiao, Y.: UniFormer: Unified
848 Transformer for Efficient Spatial-Temporal Representation Learning,
849 *International Conference on Learning Representations*, 2021b.

850 Li, L. and Wu, J.: Spatiotemporal estimation of satellite-borne and ground-level NO₂
851 using full residual deep networks, *Remote Sensing of Environment*, 254, 112257,
852 <https://doi.org/10.1016/j.rse.2020.112257>, 2021.

853 Li, M., Wang, T., Xie, M., Zhuang, B., Li, S., Han, Y., and Chen, P.: Impacts of aerosol-
854 radiation feedback on local air quality during a severe haze episode in Nanjing
855 megacity, eastern China, *Tellus B: Chemical and Physical Meteorology*, 69,
856 1339548, <https://doi.org/10/gsfjz3>, 2017.

857 Li, M., Yang, Q., Yuan, Q., and Zhu, L.: Estimation of high spatial resolution ground-
858 level ozone concentrations based on Landsat 8 TIR bands with deep forest model,
859 *Chemosphere*, 301, 134817, <https://doi.org/10.1016/j.chemosphere.2022.134817>,
860 2022b.

861 Lin, C., Huang, R.-J., Zhong, H., Duan, J., Wang, Z., Huang, W., and Xu, W.:
862 Elucidating ozone and PM_{2.5} pollution in the Fenwei Plain reveals the co-benefits
863 of controlling precursor gas emissions in winter haze, *Atmos. Chem. Phys.*, 23,
864 3595–3607, <https://doi.org/10/gsfvs3>, 2023.

865 Liu, M., Huang, Y., Ma, Z., Jin, Z., Liu, X., Wang, H., Liu, Y., Wang, J., Jantunen, M.,
866 Bi, J., and Kinney, P. L.: Spatial and temporal trends in the mortality burden of air
867 pollution in China: 2004–2012, *Environment International*, 98, 75–81,
868 <https://doi.org/10.1016/j.envint.2016.10.003>, 2017.

869 Liu, X., Shi, X., Lei, Y., and Xue, W.: Path of coordinated control of PM_{2.5} and ozone
870 in China, *Chin. Sci. Bull.*, 67, 2089–2099, <https://doi.org/10.1360/TB-2021-0832>,
871 2022.

872 Lu, D., Mao, W., Zheng, L., Xiao, W., Zhang, L., and Wei, J.: Ambient PM_{2.5} Estimates
873 and Variations during COVID-19 Pandemic in the Yangtze River Delta Using
874 Machine Learning and Big Data, *Remote Sensing*, 13, 1423,
875 <https://doi.org/10.3390/rs13081423>, 2021.

876 Lu, X., Hong, J., Zhang, L., Cooper, O. R., Schultz, M. G., Xu, X., Wang, T., Gao, M.,
877 Zhao, Y., and Zhang, Y.: Severe Surface Ozone Pollution in China: A Global

878 Perspective, Environ. Sci. Technol. Lett., 5, 487–494,
879 <https://doi.org/10.1021/acs.estlett.8b00366>, 2018.

880 Lundberg, S. M. and Lee, S.-I.: A Unified Approach to Interpreting Model Predictions,
881 in: Proceedings of the 31st International Conference on Neural Information
882 Processing Systems, Red Hook, NY, USA, 2017.

883 Lyapustin, A. and Wang, Y.: MODIS/Terra+Aqua Land Aerosol Optical Depth Daily
884 L2G Global 1km SIN Grid V061, NASA EOSDIS Land Processes DAAC,
885 <https://doi.org/10.5067/MODIS/MCD19A2.061>, 2022.

886 Miller, D. F., Alkezweeny, A. J., Hales, J. M., and Lee, R. N.: Ozone Formation Related
887 to Power Plant Emissions, Science, 202, 1186–1188, <https://doi.org/10/b5kgjr>,
888 1978.

889 Mitchell, R., Frank, E., and Holmes, G.: GPUtreeShap: massively parallel exact
890 calculation of SHAP scores for tree ensembles, PeerJ Computer Science, 8,
891 <https://doi.org/10.7717/peerj-cs.880>, 2020.

892 Myers, S. L.: The Worst Dust Storm in a Decade Shrouds Beijing and Northern China,
893 The New York Times, 15th March, 2021.

894 Pusede, S. E., Steiner, A. L., and Cohen, R. C.: Temperature and Recent Trends in the
895 Chemistry of Continental Surface Ozone, Chem. Rev., 115, 3898–3918,
896 <https://doi.org/10.1021/cr5006815>, 2015.

897 Ren, J., Guo, F., and Xie, S.: Diagnosing ozone-NO_x-VOC sensitivity and revealing
898 causes of ozone increases in China based on 2013-2021 satellite retrievals, Atmos.
899 Chem. Phys., 22, 15035–15047, <https://doi.org/10.5194/acp-22-15035-2022>,
900 2022a.

901 Ren, X., Mi, Z., Cai, T., Nolte, C. G., and Georgopoulos, P. G.: Flexible Bayesian
902 Ensemble Machine Learning Framework for Predicting Local Ozone
903 Concentrations, Environ. Sci. Technol., 56, 3871–3883,
904 <https://doi.org/10.1021/acs.est.1c04076>, 2022b.

905 Requia, W. J., Di, Q., Silvern, R., Kelly, J. T., Koutrakis, P., Mickley, L. J., Sulprizio,

906 M. P., Amini, H., Shi, L., and Schwartz, J.: An Ensemble Learning Approach for
907 Estimating High Spatiotemporal Resolution of Ground-Level Ozone in the
908 Contiguous United States, *Environ. Sci. Technol.*, 54, 11037–11047,
909 <https://doi.org/10.1021/acs.est.0c01791>, 2020.

910 Román, M. O., Wang, Z., Sun, Q., Kalb, V., Miller, S. D., Molthan, A., Schultz, L., Bell,
911 J., Stokes, E. C., Pandey, B., Seto, K. C., Hall, D., Oda, T., Wolfe, R. E., Lin, G.,
912 Golpayegani, N., Devadiga, S., Davidson, C., Sarkar, S., Praderas, C., Schmaltz,
913 J., Boller, R., Stevens, J., Ramos González, O. M., Padilla, E., Alonso, J., Detrés,
914 Y., Armstrong, R., Miranda, I., Conte, Y., Marrero, N., MacManus, K., Esch, T.,
915 and Masuoka, E. J.: NASA’s Black Marble nighttime lights product suite, *Remote
916 Sensing of Environment*, 210, 113–143, <https://doi.org/10/ghqpjh>, 2018.

917 Shapley, L. S.: A value for n-person games, in: *The Shapley Value: Essays in Honor of
918 Lloyd S. Shapley*, edited by: Roth, A. E., Cambridge University Press, Cambridge,
919 31–40, <https://doi.org/10.1017/CBO9780511528446.003>, 1988.

920 Shrikumar, A., Greenside, P., and Kundaje, A.: Learning Important Features Through
921 Propagating Activation Differences, <http://arxiv.org/abs/1704.02685>, 12 October
922 2019.

923 Sicard, P., Serra, R., and Rossello, P.: Spatiotemporal trends in ground-level ozone
924 concentrations and metrics in France over the time period 1999–2012,
925 *Environmental Research*, 149, 122–144,
926 <https://doi.org/10.1016/j.envres.2016.05.014>, 2016.

927 Sicard, P., De Marco, A., Agathokleous, E., Feng, Z., Xu, X., Paoletti, E., Rodriguez, J.
928 J. D., and Calatayud, V.: Amplified ozone pollution in cities during the COVID-
929 19 lockdown, *Science of The Total Environment*, 735, 139542,
930 <https://doi.org/10/gg5w8h>, 2020.

931 Sillman, S.: The use of NO_y , H_2O_2 , and HNO_3 as indicators for ozone- NO_x -hydrocarbon
932 sensitivity in urban locations, *J. Geophys. Res.*, 100, 14175,
933 <https://doi.org/10.1029/94JD02953>, 1995.

934 Song, H., Lu, K., Dong, H., Tan, Z., Chen, S., Zeng, L., and Zhang, Y.: Reduced Aerosol
935 Uptake of Hydroperoxyl Radical May Increase the Sensitivity of Ozone
936 Production to Volatile Organic Compounds, *Environ. Sci. Technol. Lett.*, 9, 22–29,
937 <https://doi.org/10/gnqqb9>, 2022a.

938 Song, K., Liu, R., Wang, Y., Liu, T., Wei, L., Wu, Y., Zheng, J., Wang, B., and Liu, S.
939 C.: Observation-based analysis of ozone production sensitivity for two persistent
940 ozone episodes in Guangdong, China, *Atmos. Chem. Phys.*, 22, 8403–8416,
941 <https://doi.org/10/gr4qz2>, 2022b.

942 Souri, A. H., Johnson, M. S., Wolfe, G. M., Crawford, J. H., Fried, A., Wisthaler, A.,
943 Brune, W. H., Blake, D. R., Weinheimer, A. J., Verhoelst, T., Compernelle, S.,
944 Pinardi, G., Vigouroux, C., Langerock, B., Choi, S., Lamsal, L., Zhu, L., Sun, S.,
945 Cohen, R. C., Min, K.-E., Cho, C., Philip, S., Liu, X., and Chance, K.:
946 Characterization of errors in satellite-based HCHO/NO₂ tropospheric column
947 ratios with respect to chemistry, column-to-PBL translation, spatial representation,
948 and retrieval uncertainties, *Atmospheric Chemistry and Physics*, 23, 1963–1986,
949 <https://doi.org/10.5194/acp-23-1963-2023>, 2023.

950 Su, W., Hu, Q., Chen, Y., Lin, J., Zhang, C., and Liu, C.: Inferring global surface HCHO
951 concentrations from multisource hyperspectral satellites and their application to
952 HCHO-related global cancer burden estimation, *Environment International*, 170,
953 107600, <https://doi.org/10.1016/j.envint.2022.107600>, 2022.

954 Sun, H., Shin, Y. M., Xia, M., Ke, S., Wan, M., Yuan, L., Guo, Y., and Archibald, A. T.:
955 Spatial Resolved Surface Ozone with Urban and Rural Differentiation during
956 1990–2019: A Space–Time Bayesian Neural Network Downscaler, *Environ. Sci.*
957 *Technol.*, 56, 7337–7349, <https://doi.org/10.1021/acs.est.1c04797>, 2022.

958 Tan, Z., Lu, K., Ma, X., Chen, S., He, L., Huang, X., Li, X., Lin, X., Tang, M., Yu, D.,
959 Wahner, A., and Zhang, Y.: Multiple Impacts of Aerosols on O₃ Production Are
960 Largely Compensated: A Case Study Shenzhen, China, *Environ. Sci. Technol.*, 56,
961 17569–17580, <https://doi.org/10/gsgp79>, 2022.

962 Tang, L., Xue, X., Qu, J., Mi, Z., Bo, X., Chang, X., Wang, S., Li, S., Cui, W., and Dong,
963 G.: Air pollution emissions from Chinese power plants based on the continuous
964 emission monitoring systems network, *Sci Data*, 7, 325, <https://doi.org/10/ghfqf>,
965 2020.

966 Tao, C.: Surface Ozone, NO₂, and PM_{2.5} Concentrations Estimated by the Deep
967 Learning model (Air Transformer) based on Satellite data,
968 <https://doi.org/10.5281/zenodo.10071408>, 2023.

969 Thongthammachart, T., Araki, S., Shimadera, H., Matsuo, T., and Kondo, A.:
970 Incorporating Light Gradient Boosting Machine to land use regression model for
971 estimating NO₂ and PM_{2.5} levels in Kansai region, Japan, *Environmental*
972 *Modelling & Software*, 155, 105447,
973 <https://doi.org/10.1016/j.envsoft.2022.105447>, 2022.

974 Wei, J., Li, Z., Li, K., Dickerson, R. R., Pinker, R. T., Wang, J., Liu, X., Sun, L., Xue,
975 W., and Cribb, M.: Full-coverage mapping and spatiotemporal variations of
976 ground-level ozone (O₃) pollution from 2013 to 2020 across China, *Remote*
977 *Sensing of Environment*, 270, 112775, <https://doi.org/10.1016/j.rse.2021.112775>,
978 2022a.

979 Wei, J., Liu, S., Li, Z., Liu, C., Qin, K., Liu, X., Pinker, R. T., Dickerson, R. R., Lin, J.,
980 Boersma, K. F., Sun, L., Li, R., Xue, W., Cui, Y., Zhang, C., and Wang, J.: Ground-
981 Level NO₂ Surveillance from Space Across China for High Resolution Using
982 Interpretable Spatiotemporally Weighted Artificial Intelligence, *Environ. Sci.*
983 *Technol.*, [acs.est.2c03834](https://doi.org/10.1021/acs.est.2c03834), <https://doi.org/10.1021/acs.est.2c03834>, 2022b.

984 Wei, W., Wang, X., Wang, X., Li, R., Zhou, C., and Cheng, S.: Attenuated sensitivity of
985 ozone to precursors in Beijing–Tianjin–Hebei region with the continuous NO_x
986 reduction within 2014–2018, *Science of The Total Environment*, 813, 152589,
987 <https://doi.org/10/gq7ngn>, 2022c.

988 WorldPop: Global High Resolution Population Denominators Project - Funded by The
989 Bill and Melinda Gates Foundation (OPP1134076),

990 <https://dx.doi.org/10.5258/SOTON/WP00675>, 2018.

991 Xiao, Q., Chang, H. H., Geng, G., and Liu, Y.: An Ensemble Machine-Learning Model
992 To Predict Historical PM_{2.5} Concentrations in China from Satellite Data, *Environ.*
993 *Sci. Technol.*, 52, 13260–13269, <https://doi.org/10.1021/acs.est.8b02917>, 2018.

994 Yue, X., Unger, N., Harper, K., Xia, X., Liao, H., Zhu, T., Xiao, J., Feng, Z., and Li, J.:
995 Ozone and haze pollution weakens net primary productivity in China,
996 *Atmospheric Chemistry and Physics*, 17, 6073–6089, [https://doi.org/10.5194/acp-](https://doi.org/10.5194/acp-17-6073-2017)
997 [17-6073-2017](https://doi.org/10.5194/acp-17-6073-2017), 2017.

998 Zhang, J., Wang, J., Sun, Y., Li, J., Ninneman, M., Ye, J., Li, K., Crandall, B., Mao, J.,
999 Xu, W., Schwab, M. J., Li, W., Ge, X., Chen, M., Ying, Q., Zhang, Q., and Schwab,
1000 J. J.: Insights from ozone and particulate matter pollution control in New York City
1001 applied to Beijing, *npj Clim Atmos Sci*, 5, 85, [https://doi.org/10.1038/s41612-022-](https://doi.org/10.1038/s41612-022-00309-8)
1002 [00309-8](https://doi.org/10.1038/s41612-022-00309-8), 2022.

1003 Zhang, R., Lei, W., Tie, X., and Hess, P.: Industrial emissions cause extreme urban
1004 ozone diurnal variability, *Proc. Natl. Acad. Sci. U.S.A.*, 101, 6346–6350,
1005 <https://doi.org/10.1073/pnas.0401484101>, 2004.

1006 Zhao, M., Cheng, C., Zhou, Y., Li, X., Shen, S., and Song, C.: A global dataset of annual
1007 urban extents (1992–2020) from harmonized nighttime lights, *Earth System*
1008 *Science Data*, 14, 517–534, <https://doi.org/10.5194/essd-14-517-2022>, 2022.

1009 Zheng, B., Tong, D., Li, M., Liu, F., Hong, C., Geng, G., Li, H., Li, X., Peng, L., Qi, J.,
1010 Yan, L., Zhang, Y., Zhao, H., Zheng, Y., He, K., and Zhang, Q.: Trends in China’s
1011 anthropogenic emissions since 2010 as the consequence of clean air actions,
1012 *Atmos. Chem. Phys.*, 18, 14095–14111, [https://doi.org/10.5194/acp-18-14095-](https://doi.org/10.5194/acp-18-14095-2018)
1013 [2018](https://doi.org/10.5194/acp-18-14095-2018), 2018.

1014